Project Report

LSP-277

Self-Aware Telescope: FY19 Optical Systems Technology Line-Supported Program

T.R. Price
M.J. Silver
S.R. Trotz
P.D. Chapnik
M.A. Echter
S.K. Jeon

17 December 2019

Lincoln Laboratory

MASSACHUSETTS INSTITUTE OF TECHNOLOGY

LEXINGTON, MASSACHUSETTS

This material is based upon work supported by the Under Secretary of Defense for Research and Engineering under Air Force Contract No. FA8702-15-D-0001.

This report is the result of studies performed at Lincoln Laboratory, a federally funded research and development center operated by Massachusetts Institute of Technology. This material is based upon work supported by the Under Secretary of Defense for Research and Engineering under Air Force Contract No. FA8702-15-D-0001. Any opinions, findings, conclusions or recommendations expressed in this material are those of the author(s) and do not necessarily reflect the views of the U.S. Air Force.

Massachusetts Institute of Technology
Lincoln Laboratory

Self-Aware Telescope:
FY19 Optical Systems Technology
Line-Supported Program

T.R. Price
M.J. Silver
S.R. Trotz
Group 91

P.D. Chapnik
Group 78

M.A. Echter
Group 92

S.K.Jeon
Group 74

Project Report LSP-277
17 December 2019

Lexington Massachusetts

ABSTRACT

Large-aperture surveillance systems have used stiff, heavy structures to minimize potential distortions while on station. One then has to tolerate any residual errors. The Self-Aware Telescope approach is to develop metrology techniques to allow lightweight systems without compromising performance by monitoring changes in the primary mirror figure with strain gauges and automatically correcting those changes without the need of a separate wavefront sensor. The metering structure and petal structure utilizes sensors and actuators to maintain overall alignment of the system. Diffractive optical elements monitor the high spatial frequency errors that deformable mirrors can correct in the optical imaging package.

TABLE OF CONTENTS

LIST OF ILLUSTRATIONS

LIST OF TABLES

1. INTRODUCTION

Figure 1. Concept for 40-m Self-Aware Telescope.

Future DOD imaging system (see Figure 1) will require large telescope beyond low-earth orbit to improve persistence and resilience while maintaining or improving imaging performance. Traditionally, space telescope designs consisted of:

- High areal mass density to maintain high stiffness
- Monolithic mirror design. Occasionally, there may be designs with small number of segments
- Systems slewed to obtain star images for phase retrieval for low-order only correction

The desire exists to increase the size of spaced-based imaging assets in order to improve resolution and/or field of view. This requires segmented designs that demand advanced metrology techniques to initiate and maintain alignment. Larger apertures, approaching 40 m for GEO systems, require non-monolithic architectures because of limitations in the faring sizes, and areal densities of 10–15 kg/m^2 to stay within payload capabilities. These points to systems that are highly segmented and extremely lightweight, two features that make it difficult to maintain alignment and figure—critical to image quality. In addition, changing conditions from thermally induced distortion and mechanical loading need addressing in real time.

This Line-funded research effort sought to develop unique metrology solutions to address how to maintain the desired image quality for large lightweight-segmented imaging systems. We sought to explore four unique solutions to help address these metrology issues.

1. Embedded strain sensors to monitor changes in the shapes of the individual optical segments and truss supports
2. Diffractive optical elements (DOE) to provide high-resolution interferometric measurements of the optical surfaces
3. Distributed deformable optics to correct wavefront errors

4. Active truss supports to maintain gross alignment

The team for this project consisted of members from the Advanced Capabilities and Technologies Group (Group 91), Optical Engineering Group (Group 78), and Structural and Thermal-Fluids Engineering Group (Group 74). This report presents the progress after the first year of the program. The program did not receive funding for a second year.

2. BACKGROUND

The Hubble Space Telescope (HST) showed the efficacy of imaging with space-based telescope systems. HST is a monolithic 2.4-m primary mirror telescope (f/24) launched from the Space Shuttle, which has been on station since 1990. Assembly and alignment occurred on the ground before launch. Despite this, issues occurred with the telescope because of a mistake during the figuring of the primary mirror. An updated camera package referred to as WFPC 2 corrected this problem in 1993.

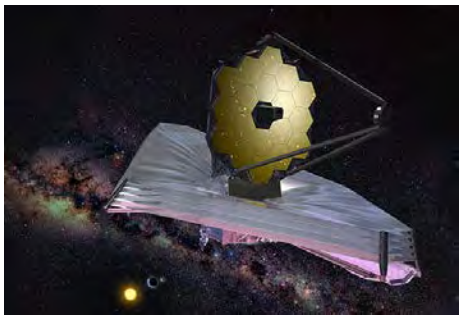

Figure 2. Rendering of JWST.

The James Webb Space Telescope (JWST) (Figure 2 and Figure 3) uses a 6.5-m primary mirror consisting of 18 hexagonal mirror segments with overall focal length of 131.4 m (f/#=20). The satellite launch is currently 2021. JWST represents a much more complex problem than HST as the telescope must be folded into a more compact package prior to launch and then opened when it is in orbit. This requires metrology to correct initially large errors in the placement of the individual segments, which must be corrected to produce residual errors of <23.7 nm rms.

Figure 3. JWST stowed within fairing.

The desire to make even larger aperture telescopes will require new techniques in order align the individual segments and maintain alignment of the entire structure. Table 1 shows notional specifications and requirements.

TABLE 1
Notional Specification and Requirements

Primary Diameter	40 meter
Focal Length	400 meter
Petal Diameter	1.5 meter
f/#	10
Petal Shape	Hex
No. of Segments	~550
Petal Control	Piston + Tilt
System Residual Error	25 nm rms
Primary Areal Density	10-15 kg/m^2

One can see the implications of the specifications outlined above. First, if the imaging package is located at the focus of a telescope lacking an obscuration, then the metering structure must be roughly 400 m long. Designers can reduce this by including an obscuration and placing the optics package behind a secondary mirror. However, this will require a larger secondary mirror that must maintain alignment

between the primary and imaging instruments. The secondary could then be a deformable mirror, but it wouldn't be located at a pupil plane, which has other performance implications. No matter the design chosen, the size of the metering structure requires controlling the structure to maintain alignment. It's not possible to make the structure sufficiently stiff to eliminate active control because of mass limitations of the launch vehicle. MIT Lincoln Laboratory chose to investigate the use of actuators to provide dynamic control of the metering structure using feedback information from embedded strain sensors.

The individual petals of the primary mirror will consist of lightweight mirror structures with a stiffening support frame on the back (see Figure 4). The mirror material could be silicon, silicon carbide, molybdenum, thin glass, or other similar material that could meet the optical requirements. Trade studies would determine the best material based on material properties, environmental conditions, and operational requirements. Figure 4 shows the initial petal concept. The optical surface has fibers attached to the back in a pattern designed to provide as much principal strain information as possible. These fibers provide strain information as intervals along their length and show the distortion of the optical surface due to factors such as heating. The support structure attached to the back of the optical surface will provide global support and the means of aligning adjacent segments. The same strain sensors on this part will show how the support bends and actuators within this structure will allow the reshaping. There will be other metrology components to measure alignment between petals to perform cophasing of the entire primary mirror.

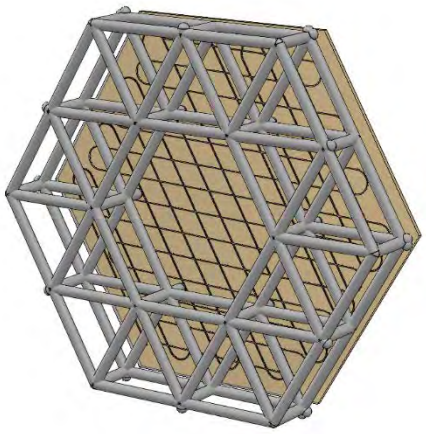

Figure 4. Initial concept of the individual primary mirror petal. This shows the back of the mirror surface, sensing fibers, and support frame.

The measurement of strain provides a relation to the deformed mirror surface through the relationship for the principal strains,

$$\varepsilon_{xx} = z\frac{\partial^2 w}{\partial x^2};\ \varepsilon_{yy} = z\frac{\partial^2 w}{\partial y^2}$$

where *w(x,y)* is the surface figure, *z* is distance from principal axis, and ε indicates the strain values. A 2D surface has three independent strain states, two orthogonal tensile-compressions strains, and a shear strain.

Strain sensors considered here are fiber-based systems that utilize either Rayleigh backscatter within the fiber or discrete fiber Bragg gratings located along with length of the individual fibers. Both these are backscatter measurements, where strain and temperature differences cause a change in the backscatter characteristics at each location. A pulsed laser source provides the means to range gate the return from different points along the fiber and so determine the locations of the fiber return. The transmitter/receiver box controls the laser and assigns locations to each of the returning pulses. The strain sensors provide a measure of the surface change do a certain level. The reconstruction algorithm and system strain resolution define the accuracy of this stage. A finer resolution measurement would provide the final error correction. The plan was to use a DOE for this step. The DOE provides petal wavefront information, which is then applied to a device such as a deformable mirror to provide the final level of correction. Errors must be within a certain range in order to be able to provide a measurement.

3. SELF-AWARE TELESCOPE CONCEPT

The concept behind the Self-Aware Telescope involves developing new metrology and control techniques to align and maintain the wavefront quality of a next-generation large imaging telescope. These would be for apertures well beyond the 6.5-m aperture of the JWST. The baseline concept calls for apertures approximately 40 m in diameter, which would produce imaging resolution of 0.5 m for a system at GEO. This program did not intend to build a device of this size, but to use appropriate specifications as an aid in the development of metrology concepts for these size apertures. The concepts under investigation are:

1. Fiber strain sensor to monitor changes in the shapes of the optical segments and truss supports.

2. DOEs to provide interferometric measurement of the optics.

3. Distributed deformable optics to perform final wavefront error correction. This would consist of both active mirror petals and an individual deformable mirror downstream from the primary.

4. Active truss supports to maintain gross alignment.

It's intended that the four items work in concert to maintain optimal wavefront quality when faced with a variable environment due to factors such as thermal loading and mechanical stress. The fiber strain sensors would measure a change in strain from a baseline value. This difference would drive a control system that would then modify the truss supports and individual primary mirror segment figure to maintain the desired wavefront quality. Depending on the final resolution of the strain sensor system, the DOE measurements would provide the final error signal needed to control the deformable mirror.

The Phase I program intended to address the following:

1. Develop notional specifications and requirements.

2. Perform laboratory tests to evaluate the use of fiber strain sensors to predict mirror shape.

3. Evaluate various strain inversion algorithms.

4. Develop finite element analysis (FEA) model of distorted optical surface for expected residual error to test reconstruction and predict expected strain values.

3.1 SPECIFICATIONS AND REQUIREMENTS

Since we are dealing with a notional system around which to develop the metrology, it is prudent to develop a set of specifications and requirements around which to base the development. Table 2 contains the justifications for the principal specifications.

TABLE 2

Notional Specifications and Requirements

Specification	Value	Justification
Primary Diameter	40 m	Provides 0.5-m resolution at GEO
Focal Length	400 m	Based on f/#
Petal Diameter	1.5 m	Based on studies of active SiC optics for large space-based imaging systems
f/#	10	Compromise between JWST value and overall size
Petal Shape	Hex	Similar to current large telescopes
No. of Segments	~550	Based on diameter and petal size
Petal Control	Piston + Tilt	Similar to current large telescopes
System Residual Error	25 nm rms	Based on HST and JWST specs
Primary Areal Density	10–15 kg/m^2	Based on studies of active SiC optics for large space-based imaging systems

3.2 STRAIN MODELING

The strain values anticipated for a typical experiment came from FEA models of the testing scenario. Preliminary Solidworks models provided an order or magnitude estimate that gave way to more detailed analysis using ABAQUS. The system modeling consisted of a thin silicon plate, either 500-μm or 1000-μm (1 or 2 wafers) thick, with three-point support around the edge. The model assumed the application of a static point force from behind generating a displacement of 10-μm Peak-to-Valley (PV; see Figure 5 and Figure 6).

The model uses the following assumptions:

- Diameter: 140 mm (circular shell)
- Material: Silicon
- Properties
    - Density: 2330 kg/m^2
    - Elastic Modulus: 112.4 GPa
    - Poisson's Ratio: 0.28
- Boundary Conditions
    - Z-Direction = 0
        - 1-mm offset rim
        - (3x) 10-mm diameter fixture points

- XY-Direction=0, Z-Rotation=0, Z-Direction =5 μm to 10 μm

- Liberally meshed at 18,760 elements

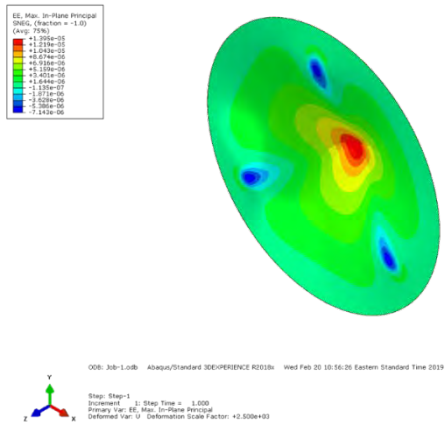

Figure 5. 1000-μm thick, 10-μm center actuation.

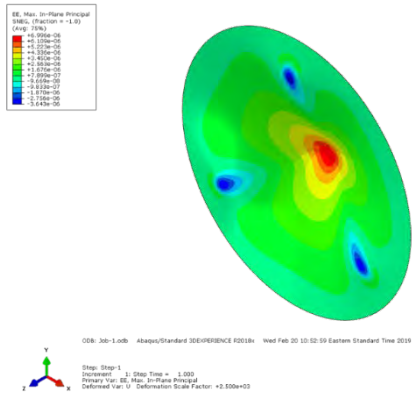

Figure 6. 500-μm thick, 10-μm center actuation.

The modeling provides multiple useful pieces of information. Not only does it show the surface with the application of a point force from behind, it also generates all the strain information needed to reconstruct the surface for comparison of different numerical techniques.

3.3 PROOF-OF-PRINCIPAL STRAIN MEASUREMENTS

The program developed a set of testing specifications for various planned proof-of-principal experiments. This helped to identify strain sensors that would have sufficient resolution to measure the expected strains. Expected strain values for the test system along with the resolution of candidate devices helped to define the test requirements.

There was a comparison of three strain gauge vendors, Luna, HBM, and Sensuron. The Table 3 outlines the identified requirements and the capabilities of each of the devices.

TABLE 3
Specification Comparison of Candidate Devices

Description	Required	Luna ODiSI 6102	HBM FS22	Sensuron RTS125
Gage Length	<1 mm–2.6 mm (adjustable with software)	0.65, 1.3, 2.6 mm	46 mm (fixed) variable only with custom fiber	6.3 mm (min)
No. of Channels	1–4 (user upgradeable)	1,4, or 8	1,4,or 8	8
Measurement Rate (min) Hz	250	250 Hz (w/ Rayleigh accelerator)	1000 Hz/50 Hz	100 Hz
Dynamic Range	±12,000 με	±12,000 με		±17,500 με
Max Gages/m/Fiber	>1,500	1538	31/127	158
Sensing Length	10–50 m	10–50 m	0.6 m	104 m

Items in green met or exceeded the specification, while red items failed to meet the requirements. The procurement selected the Luna ODiSi 6102. A Luna loaner unit performed the testing until it was possible to procure the actual device. The Appendix includes information on all three devices.

The Luna ODiSi system utilizes standard glass fibers that have been factor calibrated with regard to gage position and strain. Luna uses a Rayleigh backscatter technique to obtain the strain and temperature information needed to properly calibrate the system. A pulsed laser source generates the necessary pulse and then imperfections within the fiber scatter the laser light back to the detectors. Time-of-flight measurements allow the determination of exactly where along the fiber length the signal originated. By trading off signal strength and frequency response, the gage length and location is determined.

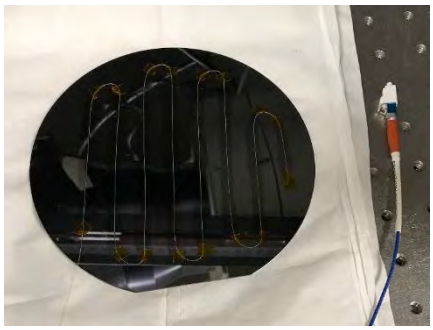

Figure 7. Silicon wafer with strain fiber bonded to back. Interface connector to the control unit sits to the right.

The experiment consisted of a standard silicon wafer 150 mm in diameter and 500 μm thick. The wafers were off-the-shelf items polished to a semiconductor grade. The thin wafer bowed easily without breaking but within the regime needed for these systems. For the initial tests, a single calibrated fiber bonded to the back served as the strain sensor. The bond pattern resembled a racetrack as seen in Figure 7. A cyano-acrylate glue bonded the straight sections of the fiber to the wafer along the length of the fiber. This placed the fiber in close contact with the wafer over the entire bonded length. There is approximately 10 mm spacing between each of the straight sections. Bonding does not occur where the fiber bends, to eliminate ambiguity in the measurements. The attempt is to measure only strain in a single direction in order to be able to differentiate strain in the direction of the principal axes. In this configuration, strain measurement occurs only along the straight sections of the fibers, resulting in either ε_{xx} or ε_{yy} strain, depending on how one wanted to define the coordinate system.

The experiment consisted of mechanically deforming the silicon wafer, then measuring the change in strain. A Zygo interferometer measured the optical surface of the wafer. The Zygo surface measurement allowed a direct comparison between the surface reconstructed from the strain measurements. Because of the thinness of the wafer, when held in a vertical position, bowing will occur causing a dense fringe pattern that can fall outside the range of the interferometer. A repeatable surface measurement over approximately 100 mm results through the positioning of the wafer and adjusting the tension on the retaining ring. This acts as a reference measurement. The surface won't be flat, but it will be within the range of the Zygo. All these factors come together to accomplish the experiment.

3.3.1 Techniques

The proof-of-principal experiment simulates the case of a thin mirror assembly that will undergo shape change when exposed to changes in environmental conditions such as heating/cooling and vibration. A commercial silicon wafer provides an excellent simulation because of the highly polished surface, high tensile strength, and ability to bend easily from to a moderate point source force. Strain measurements in one direction come from a sensor fiber bonded to the back of the silicon wafer in a repeated S-pattern. One eliminates the contributions from the curved areas by not bonding the fiber turns to the wafer.

A central part of the initial experiment is connecting measurements made by the Zygo with the fiber strain measurements. Since the Zygo is easily spatially calibrated, by measuring the extent of the interferometer measurement aperture, it's necessary to make a connection between the positions of the individual measurement along the fiber with their X and Y locations on the back of the silicon wafer. When the fibers were bonded, the straight sections remained parallel and spaced approximately 10 mm apart. Measurements located the position of the parallel fibers relative to the edge of the same side of the wafer. Measurements located the beginning and ending of each of the fibers relative to a grid on the back of the wafer. These measurements referenced against the center of the wafer. See Appendix A.3 for details.

It's then required to anchor the strain measurements along the length of the fiber with the physical location of the fiber on the back of the wafer. A 2.5-mm gauge spacing defined the location of each of the individual measurements made by the Luna device. Appendices A.2 and A.3 provide details on this process.

3.3.2 Testing

The proof-of-principal experiment desired to demonstrate that for expected distortion conditions, strain values would be measurable along with simultaneous Zygo measurements. The experiment consisted of a strain gauge instrument silicon wafer mounted in front of a 6” Zygo interferometer. A micrometer positioned behind the wafer displaces the wafer generating strain and subsequent wafer distortion. The Zygo measures the distortion allowing direct comparison between this figure and the figure reconstructed from the strain measurements.

Setup

The details of the optical setup appears in Figure 8 and Figure 9. The instrumented silicon wafer resides within a standard 6” optical mount. It’s held lightly in place by three tabs that screw into the optics mount that hold it up against the lip of the mount. The tabs are as loose as possible to minimize the introduction of bending moments into the wafer.

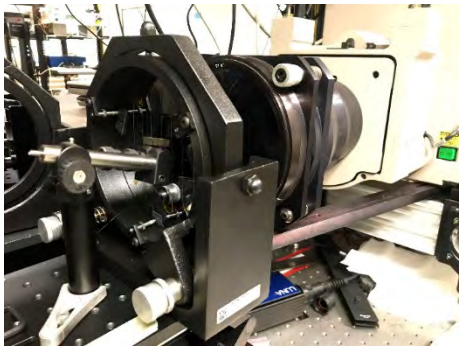

Figure 8. View of the optical setup with the 6” Zygo to the right and the 6” mount with instrumented wafer to the left. The micrometer setup sits on a post behind the optical mount.

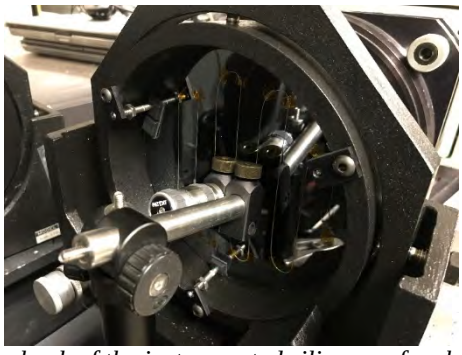

Figure 9. Close-up view of the back of the instrumented silicon wafer showing the micrometer fixture.

A micrometer stage resides behind the wafer. It utilizes a post, rod, and clamp to place the tip of the micrometer at the center of the wafer. Zygo measurements determine the peak-to-valley displacement of the wafer. These measurements reference against an unstrained measurement. Because the wafer is smooth

but not flat, it's necessary to adjust the tension of the screws holding the wafer in place and to zoom in the Zygo until the fringe density is low enough for an unambiguous measurement. This condition constitutes the reference measurement for comparison to all subsequent measurements to show the change in optical figure. Figure 10 shows a typical reference measurement obtained during this program. It shows primarily coma and this would be due to gravity sag of the wafer in the mount. The following figure (Figure 11) shows the resulting difference when applying a reference measurement against a subsequent measurement. It shows a residual of only 0.0032 λ rms or approximately λ/333 rms. This demonstrates the stability of the setup and the ability to generate repeatable results.

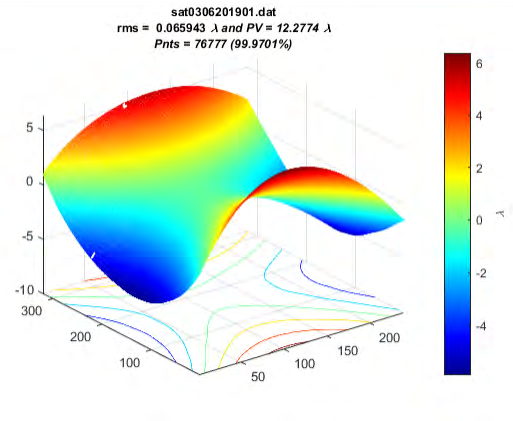

Figure 10. Zygo reference measurement of unstrained wafer. This shows 7.76 μm of wavefront error.

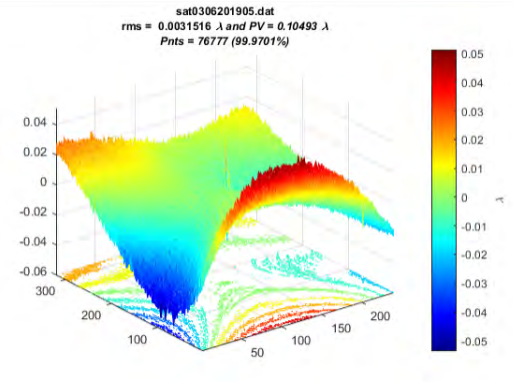

Figure 11. Zygo measurement with reference subtracted. This is showing residual of λ/333 rms. Shape probably due to miniscule vibration during measurement.

Measurement

With the setup in place, measurements proceeded with a roughly 8-μm PV surface displacement. The Zygo setup automatically subtracted a given reference measurement from the current wavefront and stored with a unique filename. Valid measurements required a full aperture along with a minimum number of valid data points, as defined by the Zygo software. An example of such a measurement is shown in Figure 12.

Appendix A.4 shows the Zernike coefficients of the deformed surface. This represents the **change** in the surface figure when the micrometer pushes from the back.

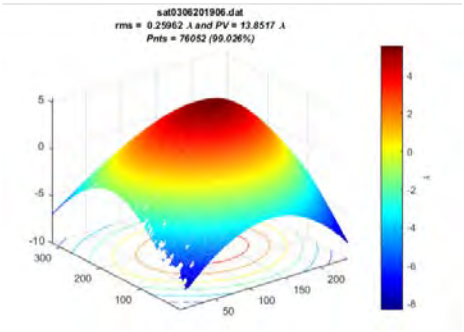

Figure 12. Zygo reference subtracted measurement of distorted wafer surface. This shows a maximum displacement of 8.8 μm PV in surface.

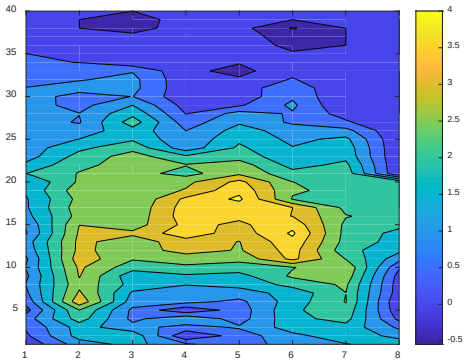

Figure 13. Contour plot of same μstrain measurement.

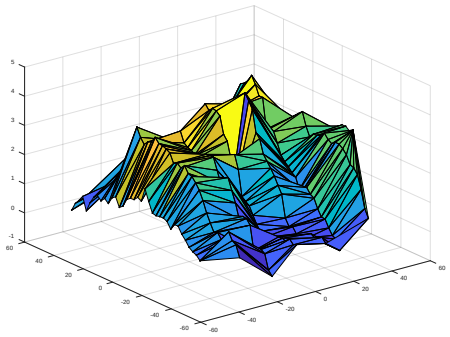

Figure 14. Surface plot of μstrain measurement.

At roughly the same time, the Luna stored the strain data from the fiber. Taring the measurement before applying the micrometer ensures that the strain measurement represents the change in strain. This ensures a match between the surface figure change and the strain change.

Measurements made during this experiment show the peak microstrain of 4.6×10^{-6} falling to roughly 2.5×10^{-6} around the edges (see Figure 13 and Figure 14). Each of the values represent an average of roughly 200 points. The standard deviation of the measurements are roughly 0.2 μstrain. Data capture occurred over a 12-s period. The initial measurements occurred with a single fiber measuring strain in a single direction. More detailed 2D strain measurements couldn't be performed because the Luna unit on loan had to be returned.

3.4 RECONSTRUCTION

The underlying idea of the program revolves around the concept that strain relates to surface deformation through a series of second order derivative equations. Strain and curvature of the surface relate through the following equations:

$$\varepsilon_{xx} = z\frac{\partial^2 w}{\partial x^2};\ \varepsilon_{yy} = z\frac{\partial^2 w}{\partial y^2};\ \varepsilon_{xy} = z\frac{\partial^2 w}{\partial x \partial y}$$

where *z* is the distance to the neutral axis, generally half the thickness of the plate under strain, and *w* is the surface deflection. This all relates to the Euler–Bernoulli beam theory.

Assuming that the basis functions are Zernike's, the surface deflection may be expanded in the basis functions so that

$$w(x_i, y_i) = \sum_j A_j Z_j(x_i, y_i)$$

When looking at the strain and curvature equations, we find that the second derivative for the *x* contribution is

$$\frac{\partial^2 w}{\partial x^2} = \sum_j A_j \frac{\partial^2 Z_j(x_i, y_i)}{\partial x^2}$$

This becomes a matrix inversion problem when formulated this way. It's a more manageable problem with orthogonal basis functions. However, the second derivate of the Zernike polynomials are not orthogonal.

It can be shown that recursive relations exist such that the second derivative of the Zernike equations may be simplified to combinations of individual Zernike functions that retain orthogonality (Zhao & Burge, 2013). In this way, the problem becomes the solution of the matrix equation to solve for the individual coefficients. Zernike polynomials, defined over a unit circle, are generally the equations of choice for optical problems because, in many cases, there are circular apertures. Legendre polynomials can provide similar solutions, but over a rectangular aperture (Grediac, 1997). All these cases require the application of appropriate boundary conditions.

A more detailed technique also uses matrix equations, but starts with the measured strain and uses Zernike polynomials as the basis functions to predict the overall strain state. Linear combinations of Zernike polynomials define the approximation of the strain, where unit Zernike strain is a function of the curvature. The strain state array can then predict the deformed shape, with appropriate boundary conditions.

The setup of the initial problem is

$$Cx = d$$

where

$$\boldsymbol{C} = \begin{bmatrix} \varepsilon_{xx,11} & \cdots & \varepsilon_{xx,1n} \\ \varepsilon_{yy,11} & \cdots & \varepsilon_{yy,1n} \\ \gamma_{xy,11} & \cdots & \gamma_{xy,1n} \\ \varepsilon_{xx,21} & \cdots & \varepsilon_{xx,2n} \\ \varepsilon_{yy,21} & \cdots & \varepsilon_{yy,2n} \\ \gamma_{xy,21} & \cdots & \gamma_{xy,2n} \\ \vdots & \vdots & \vdots \\ \varepsilon_{xx,m1} & \cdots & \varepsilon_{xx,mn} \\ \varepsilon_{yy,m1} & \cdots & \varepsilon_{yy,mn} \\ \gamma_{xy,m1} & \cdots & \gamma_{xy,mn} \end{bmatrix}$$

Strain state at point ***1***

Strain state at point ***2***

Strain state at point ***m***

$$\boldsymbol{d} = \begin{bmatrix} \bar{\varepsilon}_{xx,1} \\ \bar{\varepsilon}_{yy,1} \\ \bar{\gamma}_{xy,1} \\ \bar{\varepsilon}_{xx,2} \\ \bar{\varepsilon}_{yy,2} \\ \bar{\gamma}_{xy,2} \\ \vdots \\ \bar{\varepsilon}_{xx,m} \\ \bar{\varepsilon}_{yy,m} \\ \bar{\gamma}_{xy,m} \end{bmatrix}$$

Measured strain at point ***1***

Measured strain at point ***2***

Measured strain at point ***m***

and

$$x = \begin{bmatrix} Z_1 \\ Z_2 \\ \vdots \\ Z_n \end{bmatrix}.$$

Assuming a linear structure and superposition applies, this system of equations can approximate the strain state of the entire surface as a linear combination of Zernike unit strain functions, or even other basis functions, as shown later. Suppose there is a set of measurement points across a surface of interest, where, for the sake of simplicity, all three strain states at each point can be measured and be described as a measured strain vector, *d*. The values of matrix *C* along a column correspond to the unit Zernike strain coefficients for a Zernike mode, while each row is the unit Zernike strain coefficient for at each measurement point corresponding to the measured strain vector. The system is solved via a least-squares fit to a set of *n* Zernike

unit strain function scalars (x). With the solution, the strain state at any point on the surface may now be computed by a sum of Zernike unit strains at those points multiplied by their contributing scalars.

With the strain states defined, each strain vector has an associated displacement vector, u_z, that determines the shape of the surface. However, strain and displacement do not relate directly, but like continuum mechanics models, they relate upon adding boundary conditions. With boundary conditions, the equation is

$$\begin{bmatrix} C \\ C_u \end{bmatrix} x = \begin{bmatrix} d \\ d_u \end{bmatrix}$$

where

$C_u = \begin{bmatrix} u_{z,11} & \cdots & u_{z,1n} \\ \vdots & \ddots & \vdots \\ u_{z,j1} & \cdots & u_{z,jn} \end{bmatrix}$ is the unit Zernike z-displacements at boundary locations and

$d_u = \begin{bmatrix} \overline{u_{z,1}} \\ \vdots \\ \overline{u_{z,J}} \end{bmatrix}$ is the enforced z-displacement at boundary locations.

With this structure in place, a solution now automatically resolves the rigid body translations and rotations. In addition, weighting of C_u can strengthen or weaken its influence on the least-square solution. Shape prediction is only as good as how well the Zernike functions fit. The ability to increase the number of relevant basis functions will help immensely to decrease the fitting error.

It should be noted that a 2D surface has three independent strain states; ε_{xx}, ε_{yy}, χ_{xy}. These are the two orthogonal tensile-compression strains and a shear strain. Alternately, one can use two principal strains and their directions that still constitute three distinct states. One can technically determine the surface shape without having all three strain states, but it's only as good as the basis functions. Without all three states, the solver has a harder time detecting anomalies resulting in higher sensitivity to outliers.

With 1D sensors (such as a fiber strain gauge), it's necessary to measure strain in at least three independent directions to resolve all three strain states. Similar to a strain gauge rosette, this is possible by having three separates fibers bonded to the back of the device and oriented with two orthogonal and the third at 45°, or equally spaced at 120° from each other.

This is approach depends on how adequately the set of basis functions used can approximate the shapes of the expected surface deformation. Zernike functions are useful for optical applications as they reproduce the principal optical aberrations, but mechanical surface deformations are not necessarily optical figures. This makes Zernike somewhat limited in predicting accurate deformations of an optical surface, but should be limited to first-order fits. Ideally, the basis functions would all accurately describe potential shapes and be independent and orthogonal to one another. The use of specific structural mode shapes with the same boundary conditions provides a unique and viable starting set. The mechanical properties of the mirror generate the mode shapes through an FEA. In general, the more representative the basis functions used to the expected deformations, the more accurate the prediction becomes. For an optical application,

the approach taken here is to couple Zernike functions with the relevant structural modes. Mathematically, all these ideas combine to the following equations.

$$\begin{bmatrix} C_f\, M_f \\ C_u M_u \end{bmatrix} \begin{bmatrix} x \\ y \end{bmatrix} = \begin{bmatrix} d_f \\ d_u \end{bmatrix}$$

where x is the Zernike basis function scalars, y is the structural mode basis function scalars, d_f is the measured fiber strain,

$C_f = \begin{bmatrix} \varepsilon_{f,11} & \cdots & \varepsilon_{f,1n} \\ \vdots & \ddots & \vdots \\ \varepsilon_{f,m1} & \cdots & \varepsilon_{f,mn} \end{bmatrix}$ denotes the transformed unit strain to fiber directions of n Zernike functions, and

$M_f = \begin{bmatrix} \varepsilon_{f,11} & \cdots & \varepsilon_{f,1p} \\ \vdots & \ddots & \vdots \\ \varepsilon_{f,m1} & \cdots & \varepsilon_{f,mp} \end{bmatrix}$ denotes the direction unit strain of p structural modes.

These equations allow solving for C_f and M_f knowing d_f, d_u, x, and y using least-squares techniques.

However, it should be noted that this solution approach is not limited to optical surfaces only. It can be easily extended to predicting the deformed shape of general linear structures. One could use only structural modes or couple structural modes with static or thermal FEM load cases, instead of the special optical use-case for Zernike functions. Although the presented approach relies on the superposition of linear systems to work, it is feasible that it could be extended to nonlinear structures. At this time, it is unknown what would be required to do so, but it is suspected that one can lean heavily on nonlinear finite element theory as it seems to be quite compatible.

3.4.1 Analysis

Using the least-squares equations described previously, FEA-based simulations assessed how well the concept works. An ideal situation provided the initial proof-of-concept analysis. This consisted of a 1 mm circulate plate with 5-µm center formation. There were 164 fiber measurement points arranged in three unique directions (0, 60, -60) in an S-pattern grid (Figure 15). There was zero sensor variation and no noise. The basis functions consisted of the first 36 Zernike modes and first 6 structural modes as defined by the FEA model. The results (Figure 16 and Figure 17) showed a deformation difference ranging from -0.02–0.27 µm (0.29 µm PV). Detailed analysis shows the accurate prediction of all three-strain states. The center shows some discrepancy because the structural mode basis functions do not capture this point. To gain a better fit, more structural mode basis functions could be included that constrains the center actuation point, so the solver can more tightly account for the strain details around the actuation point.

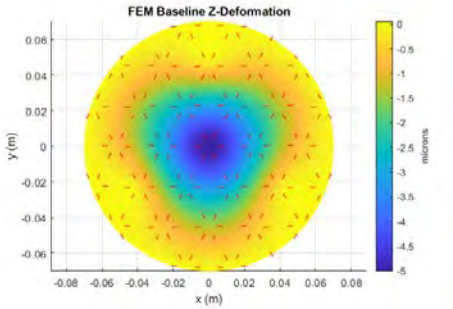

Figure 15. FEM baseline z-deformation.

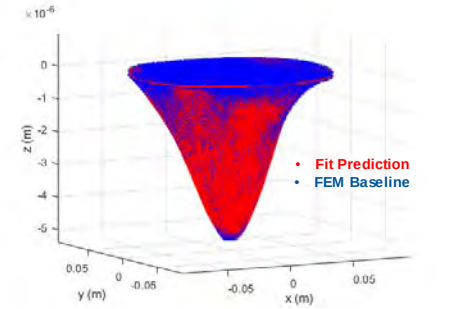

Figure 16. Deformation comparison.

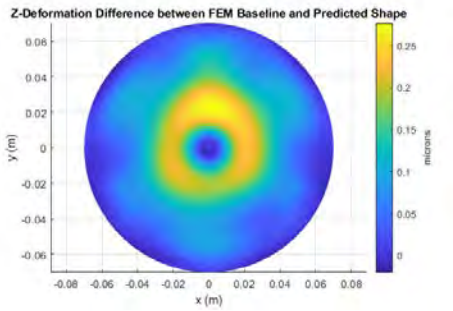

Figure 17. Difference between FEM baseline and predicted shape.

Effect of Noise

With the inclusion of random normal distribution error sensor noise (σ=1e^{-6} µm), deformation difference increases slightly (-0.25–0.27 µm, as seen in Figure 18). The high number of fiber sensors limit the effects of the noise along with even distribution and measurement in three directions.

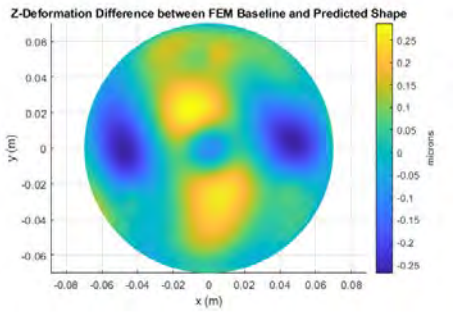

Figure 18. Z-deformation difference with the addition of random sensor error.

Reduced Number of Sensors

The next analysis step involved reducing the number of fiber sensors from 164 to 42. The directions and grid remained the same and there was no noise present. As previously, the basis functions consisted the first 36 Zernike modes and first 6 structural modes. As expected, accuracy decreased but was still very good. Deformation difference ranged from -1.0–0.1 µm (1.1 µm PV). The detailed results appear in Figure 19, Figure 20, and Figure 21.

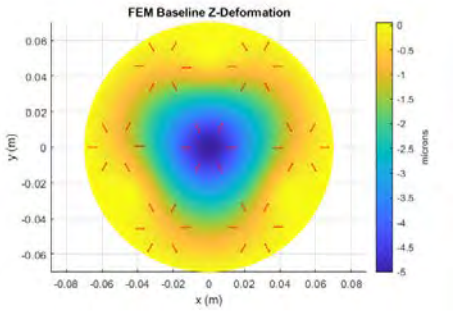

Figure 19. FEM baseline z-deformation with 42 fiber sensors.

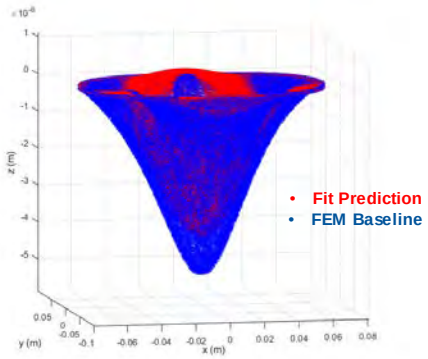

Figure 20. Deformation comparison with 42 fiber sensors.

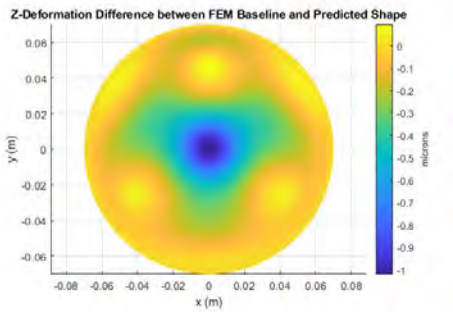

Figure 21. Deformation difference between FEM baseline and predicted shape with 42 fiber sensors.

Reduced Number of Sensors with Noise

Finally, there is added random normal noise distribution to each fiber sensor. Noise standard deviation was $1e^{-6}$ microns. In this case, there is an rms deformation difference of 0.024 µm with a range of -1.0–0.4 µm (1.4 µm PV) as seen in Figure 22. The sensor error starts to manifest as localized shape aberrations, but with not much change in the overall fit difference.

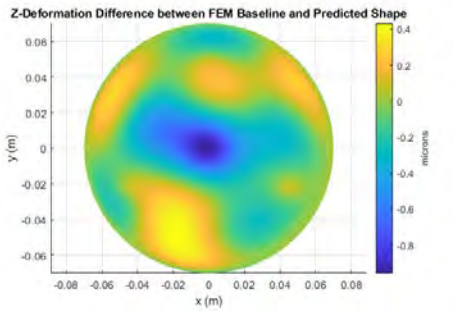

Figure 22. Deformation difference between FEM baseline and predicted shape with 42 fiber sensors and sensor noise present.

This page intentionally left blank.

4. SUMMARY

The work in the first year of the Self-Aware Telescope Line Proposal developed the necessary concepts and proof-of-principle experiments to show the viability of the concept. Specifications and requirements provide a baseline for future work and the strawman concept shows a path forward if more work is desired. The single-axis strain measurements showed measurement of strain with sufficient signal-to-noise at distortion levels expected for a larger-scale system. Identification of the basic reconstruction process occurred and showed validation using FEA models. Work needs to be done to compare actual measurements of multiple direction strains with surfaces reconstructed using this process. With this in hand, the experiment can make direct comparisons to Zygo measurements to validate the technique and provide insight into where it would begin to break down.

This page intentionally left blank.

5. REFERENCES

[1] Grediac. (1997, July 10). Method for surface reconstruction from slope or curvature measurements of rectangular areas. *Applied Optics, 36*(20), 4823-4829.

[2] Zhao, C., & Burge, J. H. (2013, Dec 12). Orthonormal curvature polynomials over a unit circle: basis set derived from curvatures of Zernike polynomials. *Optics Express, 21*(25), 31430-31443.

This page intentionally left blank.

APPENDIX A: LABORATORY STRAIN MEASUREMENT INFORMATION

A.1 SILICON WAFER PROCUREMENT

The following is the quote for the silicon wafers used in the laboratory experiment. Item # BC79114 was procured for the program. The quotation outlines the specification for the wafer.

NOVA ELECTRONIC MATERIALS

"Your Shining Star for all your Silicon and Cleanroom needs"

1189 Porter Rd. Flower Mound, 75022 TX PH: 972-478-7002 FAX: 972-478-7110

WEBSITE: WWW.NOVAWAFERS.COM E-MAIL MLightfoot@novawafers.com

QUOTATION

NAME/ADDRESS
Tom Price MIT Lincoln Laboratory 781-981-1765

DATE	QUOTE#
10/23/18	**102318-MITLL/TP**

Good day! We appreciate you giving NOVA the opportunity to quote on your needs. Please see the following options we have to offer at this time. Do not hesitate to contact us with any questions or for further assistance. As always, we look forward to being of service to you and hearing from you soon!

QTY	DESCRIPTION	PRICE EACH	TOTAL
25 wfrs (min)	**Item #7329: 4" N <100> 1-100 ohm-cm; 500-550µm Thick DSP Prime Grade Si wafers w/Primary Flat Only**	**$26.00**	**$650.00**
25 wfrs (min)	**Item#BC79114: 4" P <100> 1-10 ohm-cm; 500-550µm Thick DSP Si wafers w/2 Semi-Std. Flats**	**$24.00**	**$600.00**
Submitted by		Melanie Lightfoot - Sales Mgr.	
• **ESTIMATED SHIP DATE**		Items 1&2: 1-5 Days ARO	
• **PAYMENT TERMS**		Net 30 Days	
• **SHIPPING TERMS**		FOB: Flower Mound, TX	
• **QUOTATION VALID FOR 30 DAYS/MATERIAL AVAILABILITY FROM:**		10/23/18	

A.2 STRAIN SENSOR ATTACHMENT

Bonding of the fiber to the back of the silicon wafer proceeded using recommendations from the manufacturer. Fiber bonding utilizes a cyanoacrylate adhesive to provide moderately strong bonds that cured quickly. We used manufacturer's recommendations for how to bond the fiber. An excerpt is found below. The full description may be read at https://lunainc.com/installing-fiber-strain-sensors-2/.

"Once the surface is prepared the fiber can be laid across the coupon and held in place temporarily with tape. We recommend Kapton tape dots. They hold the fiber, are small, and can be removed easily with tweezers leaving no residue. Once the fiber is routed, tap the fiber to ensure it is in contact with the surface. If the fiber is not in contact, the Kapton dots should be repositioned until the entire length of the fiber desired for strain measurement is in contact with the surface. For a coupon one would typically use a Cyanoacrylate based adhesive. A cotton swab can be used to apply the adhesive. Place a drop of adhesive on the swab and then lightly drag down the length of the fiber. You will only cover a few centimeters [an inch] at a time, but you should still be able to bond about 1 meter per minute. You want to use as little adhesive as possible; it should be nearly invisible once cured. Within a few minutes the adhesive should be cured. At this time the Kapton dots can be removed and adhesive can be applied where the dots were. Once these spots have cured the coupon can be used."

A.3 STRAIN SENSOR LOCATION

Strain measurement occurred in the measurement vs length configuration. This will capture strain measurement along the entire length of the fiber sensor at the desired logging rate. For the data described, this was a 60Hz rate. The data file consists of individual rows along the entire length of the fiber. The first row denotes the position of the strain measurement along the fiber. Each subsequent row contains the measurements for each step in time (see Figure 23). The figure shows 2.5-mm gage spacing.

Filename C:\Users\Luna\Desktop\Self-Aware Telescope\sat03062019str-2019-02-17T08;06;46.014635.txt															
First Column is Timestamp															
First Row is Length (m)															
Matrix is Strain (microstrain)															
----------	0	0.0026	0.0052	0.0078	0.0104	0.013	0.0156	0.0182	0.0208	0.0234	0.026	0.0286	0.0312	0.0337	0.0363
Average	-1.44228	-1.7949	-0.82851	-0.79569	-1.21812	-1.09822	-1.38698	-0.85144	-0.5752	-1.29149	0.882624	1.291089	-0.54698	0.695248	0.680891
Std Dev	0.172858	0.202993	0.319115	0.213747	0.186397	0.181522	0.184273	0.180975	0.16267	0.220777	0.189537	0.20438	0.238604	0.18206	0.136277
2019-02-17T08:02:51.688344	-1.36	-1.53	-0.75	-0.69	-0.64	-0.15	-0.03	0.54	0.48	-0.14	1.38	1.67	-0.46	0.49	0.39
2019-02-17T08:06:46.013775	-0.96	-1.18	0.59	0.3	-0.63	-0.57	-1.67	-1.1	-0.99	-2.22	-0.44	-0.03	-2.41	-0.69	-0.22
2019-02-17T08:06:46.073741	-0.78	-1	0.14	0.13	-0.43	-0.5	-1.18	-0.76	-0.46	-1.35	0.82	0.98	-0.73	0.75	0.94
2019-02-17T08:06:46.133708	-1.24	-1.35	-0.35	-0.45	-0.83	-0.93	-1.57	-0.97	-0.71	-1.61	0.77	0.8	-0.84	0.56	0.6
2019-02-17T08:06:46.193673	-1.35	-1.51	-0.64	-0.62	-0.91	-0.99	-1.47	-0.93	-0.63	-1.44	0.75	0.9	-0.59	0.68	0.66
2019-02-17T08:06:46.253638	-1.51	-1.7	-0.82	-0.75	-1.03	-1.06	-1.42	-0.85	-0.55	-1.35	0.77	0.98	-0.38	0.79	0.71
2019-02-17T08:06:46.313602	-1.51	-1.77	-0.9	-0.84	-1.12	-1.13	-1.49	-0.9	-0.59	-1.39	0.65	0.88	-0.52	0.75	0.68
2019-02-17T08:06:46.373569	-1.45	-1.77	-0.91	-0.87	-1.13	-1.13	-1.43	-0.86	-0.55	-1.37	0.67	0.89	-0.56	0.7	0.61
2019-02-17T08:06:46.433534	-1.48	-1.8	-0.94	-0.95	-1.23	-1.19	-1.46	-0.87	-0.56	-1.31	0.79	1	-0.44	0.77	0.65
2019-02-17T08:06:46.493499	-1.51	-1.81	-0.98	-0.97	-1.26	-1.17	-1.46	-0.89	-0.63	-1.35	0.72	0.98	-0.46	0.75	0.64
2019-02-17T08:06:46.553464	-1.51	-1.82	-0.99	-0.98	-1.27	-1.18	-1.51	-0.89	-0.64	-1.36	0.73	1.02	-0.44	0.81	0.67
2019-02-17T08:06:46.613430	-1.55	-1.87	-1.01	-0.97	-1.25	-1.14	-1.46	-0.85	-0.59	-1.28	0.76	1.03	-0.47	0.76	0.62
2019-02-17T08:06:46.673396	-1.55	-1.87	-1	-0.93	-1.21	-1.11	-1.43	-0.8	-0.55	-1.2	0.8	1.06	-0.46	0.78	0.65
2019-02-17T08:06:46.733361	-1.54	-1.82	-0.97	-0.87	-1.14	-1.06	-1.4	-0.76	-0.53	-1.16	0.84	1.11	-0.4	0.83	0.69
2019-02-17T08:06:46.793325	-1.55	-1.84	-0.97	-0.87	-1.14	-1.05	-1.35	-0.75	-0.5	-1.12	0.87	1.14	-0.41	0.8	0.69
2019-02-17T08:06:46.853291	-1.53	-1.84	-1	-0.88	-1.16	-1.07	-1.36	-0.77	-0.51	-1.11	0.89	1.18	-0.36	0.83	0.72

Figure 23. Typical strain data file showing the first few gages along the fiber length and individual timestamps

Figure 24 shows a picture of the back of the wafer along with the bonded fiber. As can be seen, because of the technique for bonding the fiber, the fiber gage directions switch for alternate legs. This must be taken into account when applying a specific wafer location to a strain measurement. The numbers indicate the individual straight fiber sections. The #1 section resides closest to the control box and the #8 farthest. Marking applied to the back of the wafer denoted the beginning and ending of where the fibers bonded to the wafer. These markings assured reproducible locations when connecting individual gage measurements to their X–Y location on the back of the fiber.

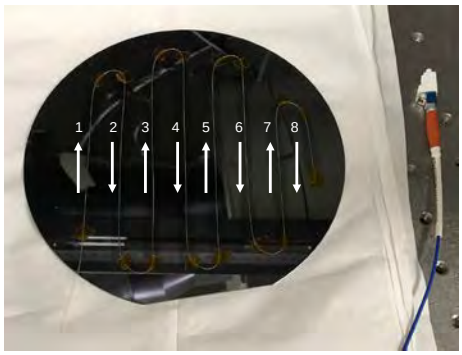

Figure 24. Layout of the fiber on the back of the wafer along with the numbering sequence and direction of the fiber.

To find the individual strain values along each of the eight fiber legs, find the column in the data file corresponding to the first gage in the list. For Leg 1, that would be 0.394588 m. Then find the column for the last gage along that path. Again, for Leg 1, that would be 0.485477 m. There is 90.9 mm of fiber along Leg 1 corresponding to 36 separate measurements. Average the individual time measurements to obtain the strain value at each of these gages. Proceed in a similar manner for each of the other sections of fiber. MATLAB code can perform this automatically.

Fiber Location	1	2	3	4	5	6	7	8
	0.394588	0.591882	0.617842	0.848884	0.869651	1.087713	1.113673	1.152613
	0.407568	0.58669	0.630822	0.835904	0.877439	1.074733	1.118865	1.209724
	0.420548	0.57371	0.643802	0.830712	0.895611	1.061754	1.137037	1.204532
	0.430932	0.563326	0.65159	0.820328	0.903399	1.056562	1.139633	
	0.443912	0.552943	0.661973	0.807348	0.911187	1.046178	1.155209	
	0.4517	0.539963	0.669761	0.796964	0.924167	1.033198	1.162997	
	0.464679	0.532175	0.680145	0.789176	0.931955	1.02541	1.175976	
	0.475063	0.519195	0.690529	0.781388	0.947531	1.020218	1.18636	
	0.485447	0.506215	0.700913	0.771004	0.955319	0.99945		
		0.501023	0.711297	0.758025	0.965702	0.991662		
			0.721681	0.745045	0.97349			

Figure 25. Location of specific strain gages along the fiber and location on the back of the wafer. The beginning and end-points for each column are the relevant values. The numbers relate the position along the fiber and can be found in the individual data files at the first row.

Fiber location relative to center								
Segment	**1**	**2**	**3**	**4**	**5**	**6**	**7**	**8**
		-32	-15	-2	13			
	-45	-32	-15	-2	13	28	43	
	-45	-32	-15	-2	13	28	43	
	-45	-32	-15	-2	13	28	43	
	-45	-32	-15	-2	13	28	43	58
	-45	-32	-15	-2	13	28	43	58
	-45	-32	-15	-2	13	28	43	58
	-45	-32	-15	-2	13	28	43	
	-45	-32	-15	-2	13	28	43	
	-45	-32	-15	-2	13	28	43	
	-45	-32	-15	-2	13	28	43	
	-45	-32	-15	-2	13	28		
			-15	-2	13	28		

Figure 26. Horizontal location of individual fibers relative to the center.

Segment	**1**	**2**	**3**	**4**	**5**	**6**	**7**	**8**
		-50	-50	-50	-50			
	-40	-40	-40	-40	-40	-40	-40	
	-30	-30	-30	-30	-30	-30	-30	
	-20	-20	-20	-20	-20	-20	-20	
	-10	-10	-10	-10	-10	-10	-10	-10
	0	0	0	0	0	0	0	0
	10	10	10	10	10	10	10	10
	20	20	20	20	20	20	20	
	30	30	30	30	30	30	30	
	40	40	40	40	40	40		
			50	50	50	50		

Figure 27. Vertical location of individual fibers relative to the center.

A.4 ZERNIKE BREAKDOWN OF ZYGO STRAIN MEASUREMENT

The measurement by the Zygo interferometer of the strained silicon wafer shown in Figure 12 has been broken down into its individual Zernike coefficients. A MATLAB script takes the stored Zygo file and extracts all the stored information. By using the available script ZernikeCalc.m with the surface array results in the calculation of the Zernike coefficients as seen below.

TABLE 4
Zernike Coefficient for Deformed Wafer Measurement

Zernike Coefficient Number	Coefficient Value	Description
1	-2.3875	Y-Tilt
2	-1.3544	X-Tilt
3	0.1711	Oblique Astigmatism
4	-1.9754	Defocus
5	-6.6518	Vertical Astigmatism
6	-0.1608	Vertical Trefoil
7	-1.0823	Vertical Coma
8	-1.3742	Horizontal Come
9	0.1282	Oblique Trefoil
10	0.8412	Oblique Quadrafoil
11	-.00024	Oblique Secondary Astigmatism
12	-0.2190	Primary Spherical
13	0.9481	Vertical Secondary Astigmatism
14	0.1043	Vertical Quadrafoil
15	0.1698	

Calculated using MatLab script ZernikeCalc.m.

APPENDIX B: CANDIDATE STRAIN SENSORS INFORMATION

B.1 LUNA ODISI 6000 INFORMATION

LUNA

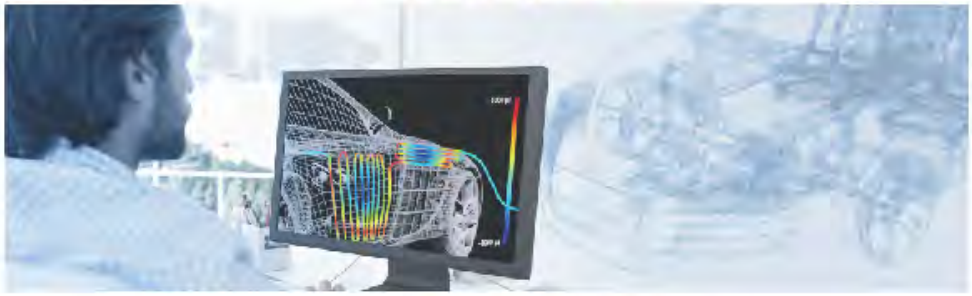

KEY FEATURES

- Multichannel measurements of strain - multiplex over 300,000 measurement locations
- Flexible, lightweight and easy to install sensors reduce time to first measurement
- Passive, corrosion resistant, dielectric, flexible sensors go where other sensors can't - in bends, around corners, embedded inside materials
- Long sensor life - no drift or recalibration required, cycle counts $>10^7$
- Large strain range and high resolution allow for mapping of complex strain fields and large strain gradients

APPLICATIONS

- Characterize strain on/in new materials and complex structures
- Profile temperature in-situ to maximize the efficiency of critical processes
- Measure two- and three-dimensional strain fields to validate FE models
- Evaluate multi-material joining
- Embed sensors within materials to create "smart parts"

ODiSI 6100

Optical Distributed Sensor Interrogator

The ODiSI is a 21st century strain and temperature measurement system specifically designed to address the test challenges of 21st century advanced materials and systems.

The ODiSI provides thousands of strain or temperature measurements per meter of a single high definition fiber sensor. The high-definition data can fully map the contour of strain for a structure under test, or the continuous thermal profile of a process, in real time.

The sensor is flexible, low profile, requires no electrical source, and can be bonded to sharply curved surfaces, embedded within structures, or mounted directly to electrical surfaces.

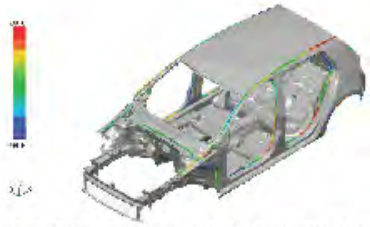

An automotive frame is instrumented with fiber and then tested under load. Test data is then superimposed on the CAD model.

www.lunainc.com | 3155 State Street, Blacksburg VA | Support phone: 1.866.586.2682 | solutions@lunainc.com

B.2 HBM FS22

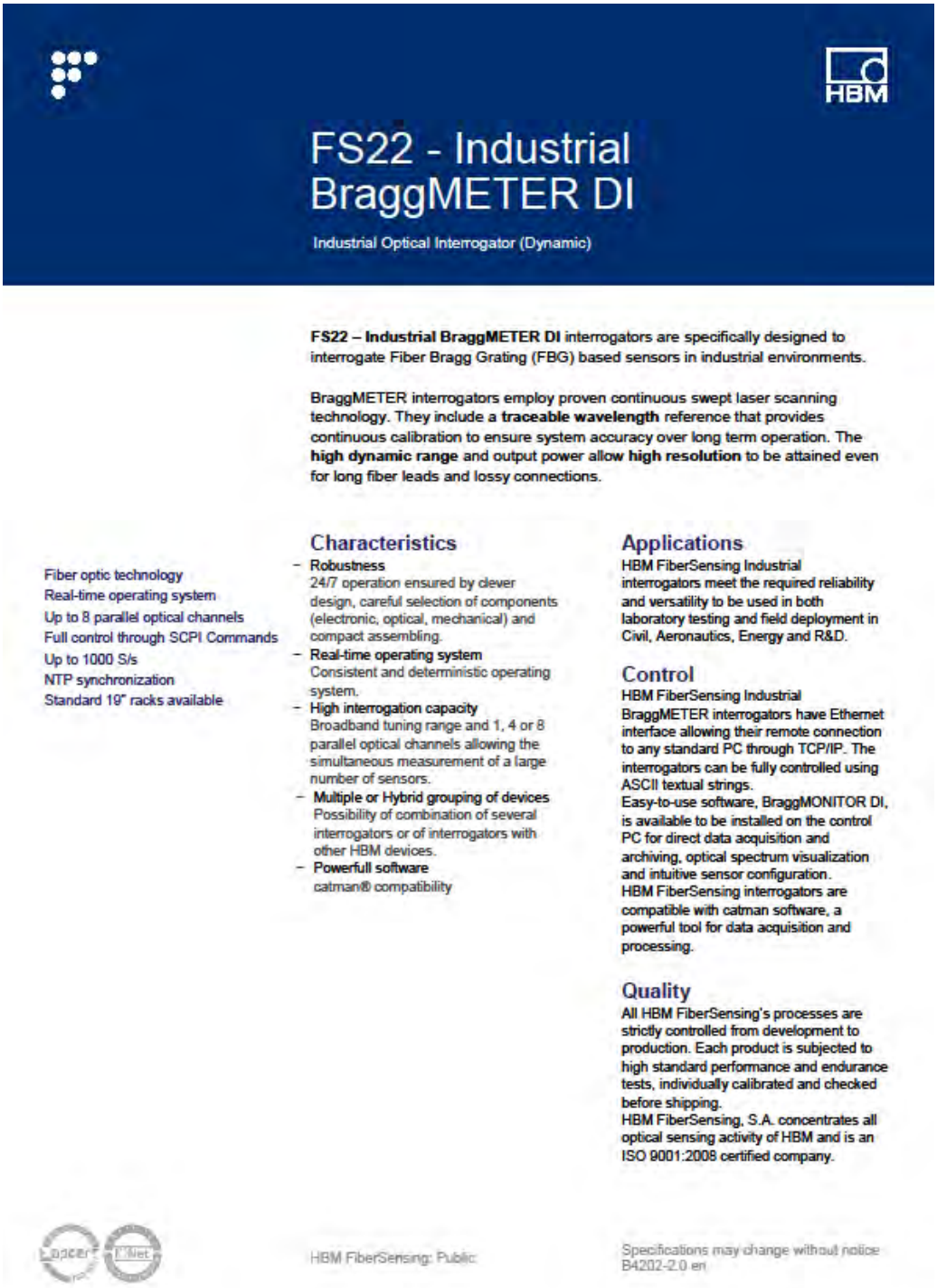

FS22 - Industrial BraggMETER DI

Industrial Optical Interrogator (Dynamic)

FS22 – Industrial BraggMETER DI interrogators are specifically designed to interrogate Fiber Bragg Grating (FBG) based sensors in industrial environments.

BraggMETER interrogators employ proven continuous swept laser scanning technology. They include a **traceable wavelength** reference that provides continuous calibration to ensure system accuracy over long term operation. The **high dynamic range** and output power allow **high resolution** to be attained even for long fiber leads and lossy connections.

Fiber optic technology
Real-time operating system
Up to 8 parallel optical channels
Full control through SCPI Commands
Up to 1000 S/s
NTP synchronization
Standard 19" racks available

Characteristics

- **Robustness**
  24/7 operation ensured by clever design, careful selection of components (electronic, optical, mechanical) and compact assembling.
- **Real-time operating system**
  Consistent and deterministic operating system.
- **High interrogation capacity**
  Broadband tuning range and 1, 4 or 8 parallel optical channels allowing the simultaneous measurement of a large number of sensors.
- **Multiple or Hybrid grouping of devices**
  Possibility of combination of several interrogators or of interrogators with other HBM devices.
- **Powerfull software**
  catman® compatibility

Applications

HBM FiberSensing Industrial interrogators meet the required reliability and versatility to be used in both laboratory testing and field deployment in Civil, Aeronautics, Energy and R&D.

Control

HBM FiberSensing Industrial BraggMETER interrogators have Ethernet interface allowing their remote connection to any standard PC through TCP/IP. The interrogators can be fully controlled using ASCII textual strings.
Easy-to-use software, BraggMONITOR DI, is available to be installed on the control PC for direct data acquisition and archiving, optical spectrum visualization and intuitive sensor configuration.
HBM FiberSensing interrogators are compatible with catman software, a powerful tool for data acquisition and processing.

Quality

All HBM FiberSensing's processes are strictly controlled from development to production. Each product is subjected to high standard performance and endurance tests, individually calibrated and checked before shipping.
HBM FiberSensing, S.A. concentrates all optical sensing activity of HBM and is an ISO 9001:2008 certified company.

HBM FiberSensing: Public

Specifications may change without notice
B4202-2.0 en

B.3 SENSURON RTS125

SENSURON
ENGINEERING AT THE SPEED OF LIGHT

RTS125+

RTS125+

Real Time Fiber Optic Sensing

Features

- Ruggedized
- 8 simultaneously monitored fiber optic sensing channels
- 2048 equally spaced sensors per fiber
- Software selectable spatial resolution down to 6.3mm.
- Real time strain and temperature measurements through FBGs
- Up to 100 Hz refresh rate
- Deflection sensing capability
- 3D shape sensing capability
- Immune to EMI/RFI and radiation for reliable operation in demanding environments.
- Networking capability via Ethernet

Benefits

- *Lifecycle Monitoring*: Monitor a product during design, development, production and operation with the same platform.
- *More Data*: Fully distributed sensing provides enough data for confident testing and model validation.
- *Multi-Sensing*: Simultaneously measure strain, temperature, deflection, 3D shape, liquid level and magnetic fields.
- *Adjustability*: The lead length is fully adjustable so users can place the sensor exactly where it needs to be.
- *Reduces Risk*: Having access to better data empowers engineers to detect design flaws earlier in product development, preventing costly failures after a product is launched.
- *Improves efficiency*: Replacing multiple technologies in a single platform, the RTS125 + allows organizations to consolidate their testing and monitoring equipment.

Application examples

- *Aerospace*: Monitor changes in wing load distribution, shape, liquid level and more in real time.
- *Automotive*: Studying truck or automobile frames to improve safety and performance.
- *Structures*: Monitoring the overall health of structures that undergo constant stress, such as bridges, dams and buildings
- *Medical*: Determining the shape of medical instruments used in non-invasive and minimally invasive surgical procedures.

www.sensuron.com/rts125

901 S Mopac • Barton Oaks Plaza Three • Ste 115
Austin • TX 78746 • USA
T +1 (512) 827-2040 • sales@sensuron.com

03/30/16

www.sensuron.com

Engineering at the Speed of Light

This page intentionally left blank.

This page intentionally left blank.